

# REPORT DOCUMENTATION PAGE

Form Approved  
OMB No. 0704-0188

Public reporting burden for this collection of information is estimated to average 1 hour per response, including the time for reviewing instructions, searching existing data sources, gathering and maintaining the data needed, and completing and reviewing the collection of information. Send comments regarding this burden estimate or any other aspect of this collection of information, including suggestions for reducing this burden, to Washington Headquarters Services, Directorate for Information Operations and Reports, 1215 Jefferson Davis Highway, Suite 1204, Arlington, VA 22202-4302, and to the Office of Management and Budget, Paperwork Reduction Project (0704-0188), Washington, DC 20503.

1. AGENCY USE ONLY (Leave blank)		2. REPORT DATE		3. REPORT TYPE AND DATES COVERED FINAL REPORT 30 Sep 91 - 29 Sep 95	
4. TITLE AND SUBTITLE Linear and Reentrant CFA S for In Situ Measurements and Comparison with Numerical Simulations and Study of Noise Mechanisms				5. FUNDING NUMBERS RS34/R5 62234N	
6. AUTHOR(S) Professor Chan					
7. PERFORMING ORGANIZATION NAME(S) AND ADDRESS(ES) Northeastern University Boston, Massachusetts 02115				8. PERFORMING ORGANIZATION REPORT NUMBER AFOSR-TR-96 0186	
9. SPONSORING/MONITORING AGENCY NAME(S) AND ADDRESS(ES) AFOSR/NE 110 Duncan Avenue Suite B115 Bolling AFB DC 20332-0001				AFOSR-91-0371	
11. SUPPLEMENTARY NOTES					
12a. DISTRIBUTION/AVAILABILITY STATEMENT APPROVED FOR PUBLIC RELEASE: DISTRIBUTION UNLIMITED				12b. DISTRIBUTION CODE	
13. ABSTRACT (Maximum 200 words)  We have performed in situ measurements in two low frequency CFAs to study several basic physics issues which may lead to CFA noise reduction. Our measurements include the local radio-frequency (RF) fields, electron density profiles, electron energy distributions and noise spectra in both the linear CFA and the reentrant CFA. Comprehensive electron density measurements of the interaction region as well as parametric comparisons such as gain versus sole voltage, beam current and frequency have been used to benchmark two computer simulation codes, MASK and NESSP.					
14. SUBJECT TERMS				15. NUMBER OF PAGES	
				16. PRICE CODE	
17. SECURITY CLASSIFICATION OF REPORT UNCLASSIFIED		18. SECURITY CLASSIFICATION OF THIS PAGE UNCLASSIFIED		19. SECURITY CLASSIFICATION OF ABSTRACT UNCLASSIFIED	
				20. LIMITATION OF ABSTRACT	

19960502 051

Final Report  
(October 1992 ~ October 1995)  
for AFOSR Grant # AFOSR-91-0371

**LINEAR AND REENTRANT CROSSED-FIELD AMPLIFIERS  
FOR *IN SITU* MEASUREMENTS, COMPARISON WITH  
NUMERICAL SIMULATIONS,  
AND STUDY OF NOISE MECHANISMS**

December 1, 1995

C. Chan, R. MacGregor, and J. Ye

Dept. of Electrical and Computer Engineering  
Northeastern University  
Boston, MA 02115

## I. PROGRAM SUMMARY

Our program contributes basic research to support the Tri-Service Vacuum Electronics' efforts on ultra low noise Crossed-Field Amplifiers (CFAs) and design for low cost. It is presently the only university program in experimental CFAs. We have performed *in situ* measurements in two low frequency CFAs to study several basic physics issues which may lead to CFA noise reduction. Our measurements include the local radio-frequency (RF) fields, electron density profiles, electron energy distributions and noise spectrums in both the linear CFA and the reentrant CFA [1], [2]. Comprehensive electron density measurements of the interaction region [3], [4], [5], [6] as well as parametric comparisons such as gain versus sole voltage, beam current and frequency [7] have been used to benchmark two computer simulation codes, MASK [8] and NESSP [9].

## II. EXPERIMENTAL DEVICE

### A. Theoretical Design

Crossed-field amplifier devices operate on the principle of energy transfer between electrons and RF electric fields. The energy transfer occurs when  $v_e \approx v_p$ , where  $v_e$  is the electron drift velocity and  $v_p$  is the RF phase velocity as seen by the electrons [2]. The electron drift velocity is controlled by the applied static electric and magnetic fields whereas the RF phase velocity is determined by the anode slow wave structure. The slow wave structure functions to retard an applied RF signal in order to match the circuit phase velocity to the electron drift velocity. Potential energy from the electrons is transferred to the RF field as the electrons bunch and drift toward the anode upon experiencing a favorable RF electric field component,  $E_{RF}$ , from the slow wave. As the electrons travel along the circuit,  $\phi$  direction for circular geometry, the RF electric field will oppose the motion of the electrons which will cause the electrons to drift towards the anode (radially outward) with velocity,  $v_r = E_{RF}/B$ , hence transferring potential energy to the field while maintaining a constant azimuthal velocity component,  $v_\phi$ . In this case, gain is observed. The RF electric field can also accelerate the electrons in which case the field transfers energy to the electrons such that the electrons are driven towards the sole electrode. Optimum performance is achieved when the electrons reach the synchronous velocity which is slightly greater than the RF phase velocity, therefore a majority of the electrons will be driven toward the anode.

The design of the experimental (linear and circular) CFA uses parameters such that diagnostic probes can be placed in the interaction region without disturbing the operation of the device (**Fig. 1**). This leads to a physically large system as described below. The frequency range of 100 MHz - 500 MHz was chosen due to the fact that the wavelength is much larger than the dimensions of the diagnostic probes. This allows for probe measurements with minimum perturbation of the electric field and space charge. As the circular device is more of a practical design, a detailed description of this device is provided. The circular device is an injected beam system in which the cathode, beam optics, and electric and magnetic fields are designed to produce a relatively smooth beam as compared to the linear CFA [1],[2]. A smooth beam may allow for more detailed measurements and studies of electron bunching and spoke formation.

## ***B. Vacuum Chamber***

The circular CFA is housed in an aluminum cylindrical vacuum chamber with O-ring sealed top and bottom plates. The chamber is 2 ft. in diameter and 2 ft. in length containing numerous ports and feeds. Some of the ports are covered with glass for visual inspection of operation and diagnostic probe status. Other ports are used for vacuum sealed feeds for movable diagnostic probes. Additional feeds are used for electrical and RF connections. The vacuum is maintained by a cryo-pump which produces a base pressure of less than  $10^{-6}$  Torr. The chamber has been designed for ease of system modification.

## ***C. Anode RF Slow Wave Structure***

As with the linear CFA [1], a serpentine line slow-wave structure is employed for the purpose of broad-band operation. A frequency range of 100 to 500 MHz is utilized for this structure. The slow-wave circuit consists of an 1/8-in diameter copper tube (water cooled) in a serpentine pattern placed on a teflon dielectric and copper ground plane. The anode circuit is 38 cm in diameter and 28 cm wide with a pitch of 1 cm. The sole is an aluminum cylinder, 15 cm wide and 33 cm diameter. The sole to anode spacing is 2.5 cm. The tube geometry is shown in **Fig. 1(b,c)**. At a typical operating frequency of 150 MHz, the slow wave wavelength is approximately 6 cm. In this case, 17 slow-wave wavelengths are included in the 102 cm peripheral length of the circuit, comparing to that of 5 slow-wave wavelengths in the linear CFA. The teflon dielectric is 2 mm thick in order to match the circuit characteristic impedance to the 50  $\Omega$  RF transmission system. The circuit stands vertically in the chamber on ceramic supports.

The RF drive source consists of a low power oscillator and a broadband amplifier capable of providing 400 W of CW power over a frequency band from 20 - 220 MHz. Directional couplers are used at the circuit input and output to provide measurement of the input forward, input reflected, and output power.

End-hats are placed 2 cm above and below each end of the sole electrode (**Fig. 1(c)**). These confining electrodes are fabricated from 1/16" thick aluminum, the lower end-hat is a fixed ring whereas the upper end-hat is a rotating disc with stainless steel screen viewing ports. The rotating disc allows for probes to be placed into the interaction region and rotated in the azimuthal direction by means of a computerized mechanical probe drive.

The magnetic field is generated by two 1 m diameter copper coils spaced 0.5 m apart, at either end of the chamber, in a Helmholtz configuration. The coils can provide up to a 350 Gauss field and are oil cooled for extended operation. Present operation utilizes an 85 Gauss field.

## ***D. Electron Source***

The device is operated as an injected beam CFA. The cathode consists of 2% thoriated tungsten filaments wrapped around an alumina rod for physical rigidity under high temperature. When the filaments are heated to emission, a 10 cm wide beam is injected into the interaction region. The cathode (-1.45 kV) is biased less negative than the sole (-2.0 kV) so that the electrons can not collect on the sole. A movable anode segment is used for further beam focusing (**Fig. 1(b)**). A similar electron source configuration has been used in the linear CFA successfully and is capable of providing up to 100 mA of electron current.

### ***E. Reentrant Drift Region***

The reentrant drift region can be modified as needed for the experiments. Electrons can be allowed to recirculate into the input region which constitutes a fully reentrant tube. A collector plate can be installed near the output end of the circuit to completely collect all electrons, hence operation in a non-reentrant format. A reentrancy controlled environment has also been designed. This configuration incorporates two segmented end-hats (approx. 4 cm in length) bounding the drift region on either end of the sole as shown in **Fig. 1(b,c)**. The segmented end-hat electrodes are connected to ground potential through a variable resistor. Varying the resistance can change the induced voltage on the segmented end-hats from the plasma potential ( $\sim -1.6$  kV), where no electrons are drawn to the end-hats, to a potential close to ground, where the electrons are depleted from the drift region in the direction of the magnetic field. The former case represents a fully reentrant regime while the latter represents a non-reentrant regime. As we can see, this configuration allows for controlled collection of electrons, hence, the ability to control the degree of re-entrancy. In this case, the drift region can function to deplete the system of possible chaotic electrons just before they reenter the interaction space. The electrons would otherwise remain circulating unless they are collected on the anode.

### ***F. Electron Density and Signal Spectrum Acquisition***

A hemispherical collection probe [1] is used to measure electron density in the interaction region. The collector is a 1 mm copper tip which is grounded through a 1 K $\Omega$  resistance. Assuming that the electrons have an average  $E \times B$  drift velocity, then the collected current is directly proportional to the time-averaged electron density. Using a hemispherical tip we can be confident of uniform electron collection from all directions. The probe is inserted through a slot in the rotating end-hat (**Fig. 1c**) and can be moved in the azimuthal direction (input-output direction) by means of a computer controlled mechanical probe drive. As the probe drive rotates the probe azimuthally, the probe voltage data is converted to digital format using an A/D converter board. Typically, 1000 data points are collected for each azimuthal (input - output) sweep, i.e. approximately 1 data point per millimeter. The probe can be moved axially to achieve different positions along the magnetic field direction (Z-direction). Also, an adjustable probe arm allows for positioning at different radial locations, allowing measurements in 3 dimensions..

The signal spectrum is acquired by the use of a General Purpose Interface Bus (GPIB) board which connects test instruments, such as spectrum analyzers, digital oscilloscopes, digital multimeters, etc., to the computer for data acquisition and control. In our experiments, we use the GPIB board to acquire spectrum analyzer data from a Tektronics 2790 series analyzer. The data acquired from the spectrum analyzer is used to derive noise power levels and signal-to-noise ratio. Software has been developed for interactive operation and ease of use.

## **II. RESEARCH HIGHLIGHTS**

### **II.1 3-D ELECTRON DENSITY MEASUREMENTS AND END-HAT EFFECTS**

We have mapped out the 3-D electron beam profiles in the linear CFA under various end-hat bias and RF drive levels (**Fig.2**). Our experiment has shown for the first time a population of electrons that are detached from the main beam when the end-hats are biased positively with respect to the sole. This

work was first reported in the Technical Digest IEDM 92 [6]. A detailed description of our end-hat experiments are published in the February 1994 issue of IEEE Transactions on Electron Devices [4]. Close collaboration with Mr. T. E. Ruden of Raytheon helped in the understanding the role of end-hat region as well as the three-dimensional effects on CFA noise performance.

## **II.2 ELECTRON RECIRCULATION**

There has long been speculations on the role of reentrant electrons in the performance, especially of the noise aspect, of CFAs. We have successfully controlled the degree of reentrancy in our circular CFA and for the first time proved the correlation between close-in noise and the amount of recirculating electrons[12]. A preliminary report of this work was published in the Proceedings of the Vacuum Electronics Annual Review, Washington D.C., June 29 to July, 1993.

As a result of this work, we gained valuable data into several unresolved issues of CFA physics. For example, the recirculating electron current was found to be roughly six times the injected beam current. Such data is also critical for benchmarking computer simulation codes. For example, it turns out that in order to achieve the level of recirculating current found in our experiment, MASK code requires extremely long running time. We are collaborating with Drs. D. Chernin and S. Riyopoulos of SAIC, Dr. H. McDowell of Varian Associates to further apply these results for the benefit of the Navy's Aegis CFA program.

## **II.3 BENCHMARKING SIMULATION CODES MASK AND NESSP**

Our research efforts have also been focused on refining and benchmarking computer simulation codes such as MASK (SAIC) and NESSP (George Dombrowski). We have experimentally verified the accuracy of these two codes in predicting the performance of the linear CFA [1], [2]. Comparisons that have been made include electron density profiles, system gain versus sole voltage, beam current and frequency (**Figs. 3-10**). The MASK code has also been used to simulate the circular CFA configured as a non-reentrant device. Good agreement has been seen between the experiment and the simulation in terms of system gain versus sole voltage and beam current. Currently, we are designing experiments to produce results that will be useful for the development of accurate numerical models for reentrant systems. We are working with Dr. D. Chernin (MASK) and Dr. G. Dombrowski (NESSP) in the code development effort.

## **II.4 NOISE AND SECONDARY ELECTRON STUDIES**

We have examined secondary yield effects with the MASK simulation code and related the results to the experimental conditions (**Fig. 11**). We have also examined noise issues experimentally and compared the results to noise production in the MASK simulation code. Noise figures were calculated using the I-Q method on waveform data acquired using a GPIB capable digital oscilloscope. Comparisons show reasonable agreement.



## II.5 DEVELOPMENT AND CHARACTERIZATION OF SECONDARY EMITTERS FOR EMITTING-SOLE CFA

The key technical issue upon conversion of the reentrant CFA from beam-injection to emitting-sole operation is to develop and maintain an active secondary emitting surface at the sole. We use the original beam-injection mechanism with altered beam optics to provide primary electron bombardment which initiates a chain reaction of secondary emission over the entire sole surface. The RF fringing field further enhances the process leading to a high density electron hub surrounding the sole. For our low power CFA, secondary emitter with both high yield and low cross-over energy is necessary.

We have developed in-house facilities for evaluation of secondary emission properties of various materials for our CFA (**Fig. 13**). Material research has been underway to develop and test new cathode materials for improved secondary yield, reliability and life-time.

Extensive studies on traditional oxide cathodes have been carried out with this setup. We have also collected fundamental data of the secondary yield for composite materials specifically developed for our CFA. These materials include field emitter arrays and hard carbon. This data was compared with some previous data for pure materials. The composite materials typically showed higher secondary yield than the related pure materials.

**Fig. 14a** shows a plot of the secondary yield for Mg and MgO. The plot shows the secondary yield coefficient as a function of impact energy for normal incidence for the pure Mg. Magnesium oxide was generated from a high temperature oxygen treatment. Significant increase in secondary yield ( $\delta$ ) shows after oxidation, with  $\delta$  reaching  $\sim 2.0$  for two hundred eV of primary energy (a typical energy of back bombardment electrons), and a maximum  $\delta$  of  $\sim 3.0$  at approximately 700 eV.

The traditional secondary emission material Beryllium-Copper is evaluated in a similar way. **Fig. 14b** is a plot of the secondary yield of the metal before and after a 4-hour Oxygen Ion Shower in an inductively coupled RF plasma. A thin oxidation layer was generated at the surface of the metal sheet. A significant increase and broadening of secondary yield peak is seen after the treatment while the primary energy for the  $\delta_{\max}$  remains about the same. As a result, the incorporation of this material into the sole was quite successful in supporting the emitting-sole CFA operation (e.g., capable of providing up to 100 mA net sole current. Detailed results will be discussed in the next section).

## II.6 EMITTING SOLE OPERATION

Our approach is to incorporate high secondary yield materials into the CFA to achieve emitting sole operation. The primary beam bombardment is provided by the electron source biased more negatively than the normal beam-injection voltage of -1.45 kV. The net sole current is monitored as an indication of emitting sole operation. The aluminum and aluminum oxide sole was used for initial testing, and found to be insufficient to provide enough secondary emission. We then examined the secondary emission properties of BeCu with various oxide layers. We found the highest secondary yield occurred after the material was oxidized using a plasma processing technique. The BeCu was processed in an inductively coupled RF oxygen plasma for a time period of four hours to achieve a secondary yield of approximately 3.9. This material was then incorporated into the circular CFA and successfully used to achieve emitting sole operation.

Basic measurements used to partially characterize the device have been completed. We have examined the electronic gain versus input power. The sole emission current was held constant at 100 mA. The results can be seen in **Fig. 15**. *In Situ* probe measurements within the interaction region have been used to show the existence of an electron hub. Radial density measurements near the output end of

the device clearly show a large increase in electron density close to the sole. Results of these measurements are also shown in Fig 15. A more detailed characterization of this operating regime is presently underway.

### III. PROGRAM RESULTS

#### III.1 LINEAR CONFIGURATION

##### III.1.1. End-Hat Effects and 3-D Electron Density Measurements

In the previous experiments, we have measured electron density profiles (time-averaged) in two dimensions, i.e., across sole-anode direction (X), and along input-output direction (Y). The results are in the form of a series of X-Y plane electron density contour plots, and can be found in [4], [5]. In this experiment, we try to map out the electron density distributions in the Y-Z plane as well as in the X-Y plane in order to get a three-dimensional picture of beam propagating in our CFA. We operated the CFA at a fixed frequency of 160 MHz under the following conditions:  $V_{\text{sole}} = -1.35$  kV,  $V_{\text{cathode}} = -1.05$  kV,  $B = 0.0052$  T, and the injected beam current was kept constant at 00 mA. The end-hat grids were biased from  $-700$  V to  $-1.4$  kV. For each end-hat bias (e.g.,  $-1.4$  kV,  $-1.2$  kV,  $-1.0$  kV,  $-800$  V and  $-700$  V), we mapped out the X-Y plane density contours with and without the RF drive signal; then the process was repeated for the other Z-positions. We typically took X-Y plane density plots in eight Z-positions in order to create a 3-D density data matrix. The contour plots are generated by MATLAB through interpolation of the measured density data.

Fig. 2 (a) shows an example of the Y-Z plane electron density contour plots; Fig. 2 (b) is a corresponding 3-D mesh plot for an overall view of the electron beam. The cut was taken at  $X = 0.6$  cm, which is close to the sole; and the end-hat was held at  $V_{\text{eh}} = -1.0$  kV. The beam starts from the electron source of 12 cm wide, and is mainly a sheath-like beam which cycloids across the DC electric and magnetic field. The width of the electron beam remains from 12 cm to 14 cm throughout the length of the interaction space at  $V_{\text{eh}} = -1.0$  kV. Along the magnetic field direction (Z-direction), the electron density profiles can be viewed as two regions. Within the range of  $|Z| \leq 6$  cm, i.e., in the middle part of the interaction space, the electron density profiles are typical of the crossed DC electric-field ( $E_x$ ) and the DC magnetic field. In this region, the density data forms closed contours that enclose higher level contours. Within the contour circle of the highest level is where the electron density peaks. The peak indicates the cusps, or turn-around points, of the cycloidal trajectories of the electrons near the sole. Note that not all of the contour levels are shown in Fig. 2. The spacing of the contour levels are chosen to simplify the visualization of the beam. A similar pattern of the density peak would re-appear while the beam propagates along the interaction space, with a spatial period approximately equal to the electron cycloidal length ( $\sim 6$  cm). This is in agreement with our previous results [3]. From  $Z \cong \pm 7$  cm to the end-hat grids ( $Z = \pm 11$  cm) is the end-hat region. In this region, the electron density either decreases monotonically towards the end-hat grids, or fluctuates. The density fluctuations are represented by high level closed contours of much smaller areas. Although the transition between the two regions is not always sharp, we can see that the fluctuations are distributed along the beam edges. These density "bumps" may represent electrons that are trapped in the end-hat region. The irregular density patterns in



the end-hat region as well as the width of the main beam vary with respect to the end-hat bias, because of the electric field non-uniformity introduced by the end-hats.

### III.2 REENTRANT CONFIGURATION

The close relationship between CFA noise performance and electron space charge recirculation has gained significant attention in tube industry. A Varian attempt found improvement in intraspectral line noise in a non-reentrant, emitting sole CFA through reduction of current recirculation [13]. Several design changes which are being investigated include an additional drift space in the Varian low noise CFA [14] and a biased control electrode in the interaction space in the Litton CFA [14]. In Northeastern University, a series of experiments have been initiated to study the role of electron recirculation on CFA performance. We have modified the reentrant CFA to include a set of segmented end-hats to collect the circulating electrons. In our experiments, we define the degree of electron beam reentrancy as the amount of electrons remain circulating in the interaction space during the amplification process. Since these electrons may carry noise memory, they may be a key reason for the poor signal-to-noise ratio commonly found in CFAs. The device characteristics have been evaluated with respect to the degree of reentrancy. It was found that the device gain and the signal-to-noise ratio are directly correlated to the degree of reentrancy. A noise reduction of  $\sim 10$  to  $12$  dB, depending upon the observation frequency, and a reduction of  $\sim 5$  dB/Hz on integrated noise power have been achieved over a  $10$  kHz single sideband close in to the carrier frequency of  $161.9$  MHz, when the electron reentrancy was varied from  $90\%$  to  $10\%$ . The anode current as well as the current collected by the segmented end-hats has also been measured as a function of reentrancy. The current measurements show that the total current collected on the RF circuit and the segmented end-hats is equal to the injected beam current. Such current balance measurements were repeated at different levels of reentrancy. The steady-state circulating current measured through a spatial density probe shows that the crossing current in the fully reentrant regime of operation increases by a factor of six in comparison with the non-reentrant regime of operation. The result of this measurement is used as a reference to determine the total run-time of MASK simulation code. Comparisons have been made between our experimental data and numerical simulation codes, MASK and NESSP. The results will be described briefly in this report.

The configuration of the reentrant CFA with the probe measuring system is shown in **Fig. 1**. This device has been operated in non-reentrant, fully reentrant, and reentrancy controlled formats. The non-reentrant configuration incorporates a collector plate at the end of the interaction region which collects all beam electrons allowing no recirculation. The fully reentrant configuration consists of the removal of the collector plate allowing all electrons to reenter the interaction space. A reentrancy controlled environment has also been designed. This configuration utilizes two segmented end-hats (approx.  $4$  cm in length) bounding the drift region on either end of the sole (**Fig. 1**). The electron current collected on the segmented end-hat electrodes induces a voltage through a variable resistor to ground. By changing the resistance value, the voltage on the segmented end-hats can be changed from the plasma potential of  $\sim -1.5$  kV, where no electrons are drawn to the end-hats, to a potential close to ground, where electrons are depleted from the drift region. The former case corresponds to a fully reentrant regime of operation while the latter corresponds to a non-reentrant regime. This configuration has been modified to include a piece of metal screen that covers each of the electrodes. The metal screen is biased  $30$  V more negative than the segmented end-hats, in order to suppress secondary emission from the electrodes. Our device has been extensively characterized in each of the three operating regimes.

### III.2.1.

#### *Non-Reentrant Experiment*

In the non-reentrant regime of operation, we have found good agreement between the experimental and simulation results. Fig. 2 shows a graph of device electronic gain versus injected beam current in this regime. The operating parameters are  $V_{sole} = -2.0$  kV,  $V_{cathode} = -1.45$  kV,  $B = 85$  Gauss, and the RF drive power is 10 W. Also, at an operating frequency of 153 MHz, approximately 17 slow-wave wavelengths are included in the 102 cm peripheral length of the RF circuit. In this regime, the circular CFA yields a 6.2 dB gain.

### III.2.2.

#### *Fully Reentrant Experiment*

Under the fully reentrant regime of operation, the device gain of the CFA increases significantly, as expected. At 10 W RF drive, we obtain a gain of 8.4 dB with an injected beam current of 30 mA, comparing to the 3.8 dB gain for non-reentrant regime under the same operating conditions. A maximum gain of 14.4 dB has been achieved for low RF drive in the reentrant operation, as shown in Fig. 3.

Our experimental work in conjunction with the work of code developers such as SAIC (MASK) and George Dombrowski (NESSP) is an important and necessary phase in the development of accurate numerical simulation models for reentrant devices. For example, an important result for code development is the experimental measurement of the steady state circulating current. The amount of electron current circulating in the interaction region is related to the lifetime of circulating electrons before they are collected by the RF circuit. The steady-state circulating current is reached as a result of the electron beam equilibrium in the interaction region. Both the amount of this current and the time scale for the electrons to reach the equilibrium are critical factors for numerical simulations such as MASK. As we know, the amount of steady-state circulating current represents the actual number of electrons that participate in the electron-RF wave interaction. The longer lifetime of electrons causes a larger circulating current when system reaches a steady state. In MASK, system performance strongly depends on the effective interaction time or run time, in terms of the number of RF cycles, in the computer code. Experimental determination of the average lifetime of electrons will determine the effective interaction time of computer codes.

Experimental investigations are under way to study the effect of reentrancy on circulating current in our CFA via *in situ* diagnostics. Fig. 4 shows an example of the electron density profiles along the interaction space. The density is obtained through a spatial density probe which is positioned in the middle of the electron stream. We can see a current density that is approximately 6 times higher than that of the non-reentrant regime of operation. Further measurements are under way to investigate the circulating current.

### III.2.3.

#### *Controlled Reentrancy Experiment*

The electron reentrancy experiments use the segmented end-hat configuration to control the electron current collection for the investigation of system performance as a function of electron beam reentrancy. The percentage of reentrancy is subsequently defined as the total beam current less the electron current collected on the segmented end-hats, i.e.,  $R = (I_{injected} - I_{collected}) / I_{injected} \times 100\%$ . Fig. 5 shows I-V characteristics of the segmented end-hat unit which confirms the operation of reentrancy control. As we can see, varying the electrode voltage (varying  $R$ ) can control the percentage of reentrancy from approximately 0% to 100%.

The measurements include system gain, noise power, electron current. **Fig. 6** shows an electron current measurement where the probe is in the middle of the main electron stream both with and without RF drive. We can see that RF drive tends to draw more electrons toward the anode, therefore decreasing the electron current collected on the density probe. The amount of current decreased seems to be independent of reentrancy. Another feature seen in **Fig. 6** is that the circulating current seems to increase with higher degrees of reentrancy, both with and without RF drive. As the degree of reentrancy increases, a stronger interaction, thus higher gain and more noise, is expected. **Fig. 7** shows an approximately linear increase of device gain, in dB's, when reentrancy increases.

Noise measurements for various degrees of beam recirculation were obtained by examining the signal spectrum from the circuit output in a 20 kHz band around the carrier. The spectrum analyzer is configured with a 20 kHz span, 1 kHz resolution bandwidth, and a 200 mS sweep rate. Typically, our measurements consist of collecting eight digitized spectra for each percentage of reentrancy, from which an average spectrum is produced. **Fig. 8** shows the results for two cases, 13% and 94% reentrant. As we can see, by comparing the two cases, the reduction in noise can be as much as 10 ~ 12 dB. Although, the gain has also been reduced from 7.2 dB to 4.1 dB, the magnitude of the reduction is approximately 1/3 that of the noise reduction. Therefore, we see that a reduction in the number of recirculating electrons does reduce the noise and hence, improve the overall system performance.

We have also examined the signal/noise power level increase (gain), in discrete 1 kHz bands, as a function of beam recirculation. To obtain this quantity, we first average both the drive signal and the amplified signal power levels over 1 kHz bands to give each signal (single sideband) as 10 discrete bands. The power level increase, in terms of dB, is now determined by subtracting the original RF drive signal levels from the amplified signal levels for the respective 1 kHz bands. **Fig. 9** shows a comparison between the 13% and 93% reentrant situations. The first three 1 kHz bands are assumed to be included in the carrier and the power level increase in these bands is desired. We can clearly see that a lower percentage of beam reentrancy results in lower noise power levels. While the carrier gain also decreases for lower percentages of reentrancy, the magnitude of the reduction is always less than that of the noise reduction. An improved signal-to-noise ratio is therefore achieved. For the percent reentrancy values between the two extreme cases compared above, the results generally fall somewhere between [12]. This technique allows us to examine and track the noise components generated in specific bands close to the carrier which may be critical to system applications such as Doppler radar.

The reentrant CFA characteristics have been examined with respect to percentage of beam recirculation. The spectrum analysis techniques along with electron density measurements demonstrated here can be used in the determination of noise sources within the device. These results will be useful for more detailed electron beam and noise studies. We are currently investigating the equilibrium recirculating beam current as well as the time scale to reach equilibrium. This information will be useful for the determination of computer computation time for simulation codes.

Our experiments are designed to explore the mechanisms and the position of the reentrant electrons in regard to noise generation and to provide useful information for the development and refinement of computer simulation models of crossed-field devices. The reentrant CFA experiments will provide useful information that could lead to low noise CFA designs as well as refining and benchmarking computer simulation codes such as MASK and NESSP.

Various experiments and numerical simulations (MASK) to further characterize the Northeastern reentrant CFA have been accomplished. The MASK model of the reentrant device requires the representation of the beam injector as an emitting surface defined on the grid which is assigned a -1.45 kV bias corresponding to the experimental condition. The slow wave structure is also modeled using the

observed experimental parameters. Experimentally, we observe a 2 dB circuit loss (insertion loss), this is modeled as a distributed loss in the code. The loss is distributed equally over the 104 circuit sections. We have also examined the effect of secondary emission in the simulation by adjusting the secondary yield coefficient of the sole material. Experimental results for gain vs. sole bias and gain vs. beam current have been compared to simulation results as can be seen in **Fig. 1**. The simulation parameters correspond to the experimental parameters with the exception of the variable secondary yield parameter. As we can see, this curve contains multiple peaks in which MASK has predicted quite well. This is a very important benchmark in the code development. According to a guiding center theory [10,11], the double gain peaks (see **Fig. 1**) which have been observed both through the experiment and in the MASK simulation could be a feedback effect of the recirculating space charge [10,11]. The voltage difference between the peaks of this curve leads to  $E \times B$  drift velocities that cause a change in the electron transit time that is equal to one RF period. This result may also be very important in the study of feedback effects on the performance of CFA's [11].

We have examined the effect of secondary emission on system performance using the variable secondary yield parameter in MASK. Simulations have been performed with secondary yields of 0, 1, and 1.5 (**Fig. 1**). We note that the simulation case in which the secondary yield equal to 1 closest matches the experimental data. Experimentally, we do predict a secondary yield of 1 due to the fact that no net sole current is observed. It appears that MASK is quite sensitive to secondary emission from the sole.

For further comparison to the MASK simulation we have examined the wideband noise. This is accomplished by calculating the signal-to-noise ratio by using the statistics of the I (In-phase) and Q (Quadrature) channel signals. We have developed an experimental technique to produce this result. The amplifier output signal is acquired from a Tektronix TDS 520A digitizing oscilloscope through a general purpose interface bus (GPIB) installed in an IBM compatible computer. The signal is then mixed with mathematical cosinusoidal signals which are in phase and 90 degrees out of phase with the input signal. Using an FFT filter, we then filter out the second harmonic, produced by the mixing operation, resulting in the I and Q channel signals. The mean and standard deviation are then calculated for each channel and the signal-to-noise ratio is subsequently defined as

$$\frac{S}{N} = 10 \log_{10} \left( 1 + \frac{\langle I_n \rangle^2 + \langle Q_n \rangle^2}{\sigma_I^2 + \sigma_Q^2} \right), \quad (1)$$

where  $\sigma_I$  and  $\sigma_Q$  are the standard deviations of the I and Q channel signals, respectively, and

$$I_n(t) = 2V_n(t) \cos(\omega t + \phi_0) \text{ and } Q_n(t) = 2V_n(t) \sin(\omega t + \phi_0) \quad (2)$$

are the in-phase and quadrature components and  $V_n(t)$  is the voltage signal on vane #n.

The output signals from the MASK simulation and the experiment are shown in **Fig. 2**. Calculations using eight experimental waveforms for the fully reentrant case show that the device signal-to-noise ratio is  $25.75 \text{ dB} \pm 1.01 \text{ dB}$  as compared the MASK result of 24.25 dB.

### III.3 EMITTING SOLE CONFIGURATION

#### III.3.1. Device Modification

The key technical issue upon conversion of the reentrant CFA from beam-injection to emitting-sole operation is to develop and maintain an active secondary emitting surface at the sole. We use the original beam-injection mechanism with altered beam optics to provide primary electron bombardment which initiates a chain reaction of secondary emission over the entire sole surface. The RF fringing field further enhances the process leading to a high density electron hub surrounding the sole. For our low power CFA, secondary emitters with relatively high yield and low cross-over energy is necessary.

Experiments have been underway to accomplish emitting sole operation in our circular CFA. Our approach is to incorporate new materials to the CFA sole. The primary beam bombardment is provided by the electron source biased more negatively than the sole electrode, this configuration allows for the adjustment of the primary bombardment energy. The net sole current is monitored as an indication of emitting sole operation. The aluminum and aluminum oxide (grade 6061, part magnesium) sole was used for initial testing, and found to be insufficient to provide enough secondary emission. We then examined the secondary emission properties of pure (grade 1100) aluminum. This material was incorporated into the circular CFA and successfully used to achieve emitting sole operation.

#### III.3.2. Device Operation

Operating parameters under this regime have been increased, as compared with previous experimental configurations [12]. The input RF power is now on the order of hundreds of watts. The electric and magnetic fields have been increased by approximately 50%. The operating sole voltage is now -3.0 kV and the magnetic field is 120 Gauss. We are now operating at approximately  $\omega/2$ . We have seen up to 150 mA of emission from the sole.

Basic measurements used to partially characterize the device have been completed. We have examined the electronic gain versus input power. The sole emission current was held constant at 100 mA. The results can be seen in Fig. 5a. *In Situ* probe measurements within the interaction region have been used to show the existence of an electron hub. Radial density measurements near the output end of the device clearly show a large increase in electron density close to the sole. Results of these measurements are shown in Fig. 5b.

### III.4. CROSSED-FIELD NOISE MECHANISMS

#### III.4.1. Operation without RF Drive

A physical mechanism of the instability associated with a static, reentrant crossed-field electron flow is the self-excitation of azimuthal space charge waves. The wavelength of the eligible oscillations satisfies  $K \cdot \lambda_K = L$ , where  $L$  is the azimuthal length of the cylindrical geometry, and  $K$  is the mode number. This relation determines the frequency of the possible oscillations assuming a match between the phase velocity and azimuthal component of the electron velocity, or  $v_{ph} = r(d\phi/dt)$ . As the electron azimuthal velocity varies across the sole-anode interaction space, the resulting oscillation frequencies also vary, i.e. oscillation frequency depends upon the position of the hub electrons which excite the wave [11]. As the magnetic field is increased the secondary hub will be confined closer to the sole surface, and based on Brillouin modeling, the frequency increases as the thickness of the Brillouin hub increases, i.e. as the magnetic field decreases. Figure 6a shows the wide band spectrum of our device operating without RF



drive. This picture shows numerous oscillations spaced approximately 8 MHz apart, also, higher power oscillations exist and are spaced approximately 45 MHz apart. Our observation has determined that the high power oscillations are very stable and the intermediate oscillations are unstable, both in terms of amplitude stability. As we operate the device in the emitting sole configuration, both primary electrons (beam injection) and secondary electrons (emission) are present. The stable high power peaks may correspond to space charge waves caused by the primary beam injection, which is a stable, controllable process. Whereas the lower power oscillations (8 MHz spacing) may very well be caused by the secondary electrons which will typically be confined closer to the sole explaining the lower frequency spacing. Also the unstable nature of the oscillations may correspond to an unstable secondary emission process. MASK simulations of this mode of operation also shows similar behavior, i.e. multiple oscillations spaced approximately 7.4 MHz apart (**Fig. 6b**).

#### ***III.4.2. The Effect of RF Drive***

At low RF drive level, the typical effect is a change in the amplitude of the oscillation lines. The amplitude of the high power oscillations ( $\Delta f \sim 45$  MHz) is suppressed by about 10 dB; while the lower power oscillations ( $\Delta f \sim 8$  MHz) are generally promoted, indicating an increase of sole secondary emission. The low power oscillations are immediately modulated by the carrier frequency, forming distinct side band. As the drive power increases, lower frequency components are suppressed and new frequency components are generated closer to the carrier. Accompanied with the high drive, sole secondary emission also increases significantly. In **Fig. 7** which shows a case of 62 W drive, new fundamental frequencies (e.g., 4 MHz) between the 8 MHz low modes emerge from a broad band spectrum sideband from 80 MHz to 140 MHz. These results set the stage for the examination of the narrow band spectrum and the effect of secondary emission.

#### ***III.4.3. The Effect of Secondary Emission on Close In Noise***

An examination of the narrow band spectrum close to the carrier reveals interesting phenomena. These experiments are designed to look at the noise levels in the output signal of the CFA for various levels of primary and secondary electron current. **Figure 8a** shows the narrow band spectrum for three operating cases, 1) 200 mA of primary current and 0 mA of secondary current, 2) 175 mA of primary current and 25 mA of secondary current, and 3) 150 mA of primary current and 50 mA of secondary current. As we can see, the noise floor increases drastically with the introduction of secondary emission, also we see distinct sideband structures forming approximately 500 kHz out from the carrier. The sideband structures become very evident as the secondary emission is increased to 50 mA. Due to the frequency offset of the sidebands, this phenomena may be caused by external mechanisms such as power supply resonances. To examine this possibility, a 2  $\mu$ F capacitor was placed in parallel with the CFA to change the loading; the results are shown in **Fig. 8b**. As we can see, the sideband structures have been suppressed, but the noise floor due to the secondary emission is still very evident. Here the noise power is calculated by averaging the spectrum power density across a noise band defined to exclude the carrier signal. We then calculated the signal-to-noise ratio (S/N) using this averaged value as the decibel value below the peak signal per unit frequency (dBc/Hz). **Figure 9** is a plot of the S/N of the circuit output as a function of the net sole emission current and the RF drive level. The range of the calculated S/N is comparable with that of a practical emitting-sole CFA. We see that, at 200 W RF drive, S/N degrades by more than 10 dB as the sole current increases from zero to 25 mA, which indicates that the participation of a small amount of secondary electrons can introduce a large amount of close-in noise. In the sole

current range greater than 25 mA, the S/N deterioration seems to stop. Beyond 50 mA sole current, data is not available at this point as to predict whether there will be a come back for the S/N.

The 200 W drive level in Fig. 9 is approximately where the reentrant amplifier system has its peak gain. Higher RF drive would result in a decreased gain due to insufficient DC beam power. At 100 W and 300 W drive level, the amplifier is at least 15 dB noisier.

#### IV. CONCLUSIONS

We have developed experimental systems that will provide insight into next generation of designs for microwave tubes, specifically crossed field amplifiers. The experimental crossed field amplifiers have also provided verification of the MASK simulation code. Comparisons of various overall device operating parameters have been made with good agreement.

The emitting sole configuration is very important due to the fact that the operating mode is that of a practical device. We have examined this configuration under various conditions and RF drive levels. Initial evidence that the secondary electron current may generate noise or modulation components close in to the carrier as a function of RF drive exists. Also, evidence of an increased noise floor with the introduction of secondary emission is very prominent. Noise in these devices can also be introduced into by external sources such as power supply interaction. Noise in crossed-field devices is very complex and can be generated by numerous sources.

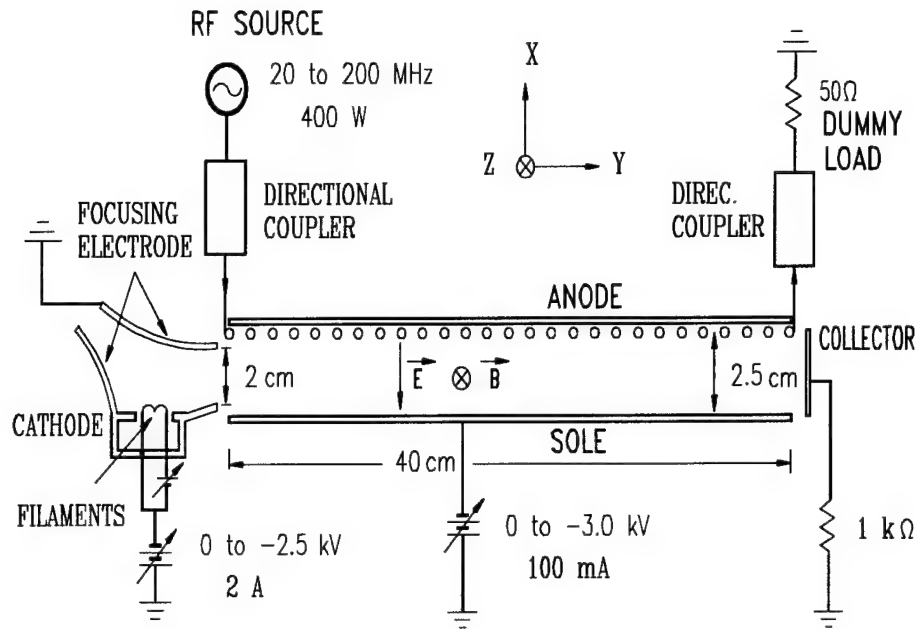
## V. REFERENCES

- [1] J. Browning, C. Chan, J. Ye, and T. E. Ruden, "A Low frequency Crossed-Field Amplifier for Experimental Investigations of Electron-RF Wave Interactions," *IEEE Trans. Plasma Science*, Vol. 19, pp. 598, 1991.
- [2] J. Browning, C. Chan, J. Ye, G. Dombrowski, and T. E. Ruden, "In situ Measurements and Numerical Simulations of Wave-Electron Interactions in a Crossed-Field Amplifier," *Appl. Phys. Lett.*, 59, pp. 3384, 1991.
- [3] C. Chan and J. Ye, "Nonlinear Interaction Between Electrons and RF Waves in Crossed Electric and Magnetic Field," *IEEE Trans. Plasma Science*, Vol. 20, pp. 659, 1992.
- [4] J. Ye, C. Chan, R. MacGregor, and T. E. Ruden, "An Experimental Investigation of the End-Hat Effects in a Crossed-Field Amplifier via 3-D Electron Density Measurements," to be appeared on *IEEE Trans. Electron Devices*, January, 1994.
- [5] J. Ye, C. Chan, R. MacGregor, and T. E. Ruden, "Crossed-Field Amplifier End-Hat Effects and 3-D Electron Density Measurements," IEEE International Conf. on Plasma Science, Vancouver, June 1993.
- [6] J. Browning, C. Chan, J. Ye, R. MacGregor, and T. E. Ruden, "Measurements of End-hat Effects in a Crossed-Field Amplifier," International Electron Device Meeting, *Technical Digest IEDM 92*, pp. 755 ~ 758, (1992).
- [7] J. Browning, C. Chan, J. Ye, T. E. Ruden, and G. Dombrowski, "Electron Plasma and Wave Measurements in a Crossed-Field Amplifier and Comparison with Numerical Simulations," *IEEE Trans. Electron Devices*, Vol. 39, pp. 2401 ~ 2407, 1992.
- [8] D. Chernin, A. Drobot, G. Hilfer, and S. Riyopoulos, "Computer Studies of Noise Generation in Crossed-Field Amplifiers," *Technical Digest IEDM 91*, pp. 593.
- [9] G. Dombrowski, "Simulation of Magnetrons and Crossed-Field Amplifiers," *IEEE Trans. Electron Devices*, Vol. 35, pp. 2060, 1988.
- [10] S. Riyopoulos, "Nonlinear Gain Computation for the Sheet Beam Crossed-Field Amplifier," To appear in *IEEE Trans. Plasma Science*, 1994.
- [11] S. Riyopoulos, "Feedback Induced Noise In Crossed-Field Devices," *IEEE Trans. Plasma Science*, Vol. 20., p. 360, 1992.

- [12] R. MacGregor, C. Chan, J. Ye, and T. E. Ruden, "A Circular Crossed-Field Amplifier for In Situ Measurements, Study of Reentrant Beam Effects, and Comparison with Numerical Simulation," to be submitted to *IEEE Trans. Electron Devices*, 1994
- [13] H. L. McDowell, "Noise Reduction in a Non-Reentrant Emitting Sole CFA," presented on Microwave Power Tube Conf., Monterey, CA, May 1992.
- [14] C. L. Wheeland, Aegis LNCFA Program Review, Waltham MA, April 2, 1992.

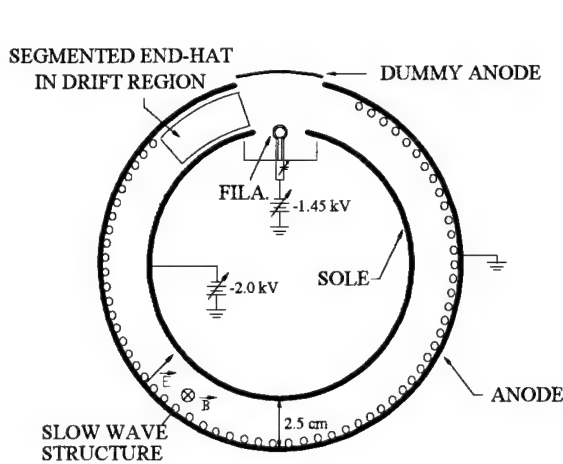


## VI. FIGURES

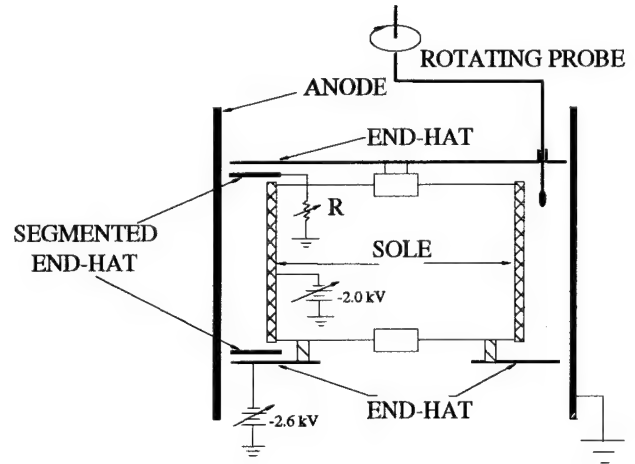


(a)

**Fig. 1** (a) The linear injected beam Crossed-Field Amplifier configuration.

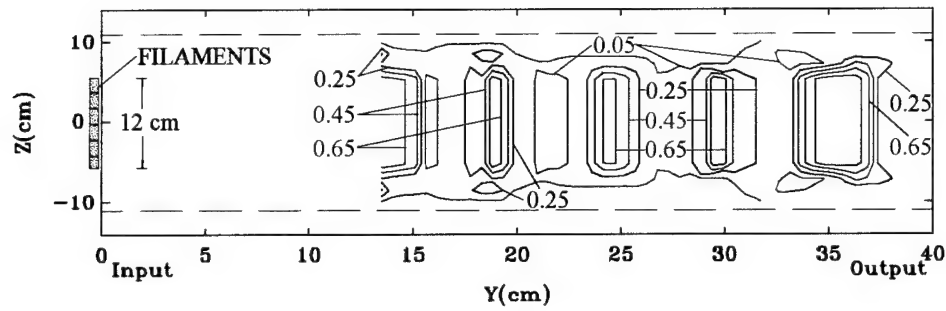


(b)

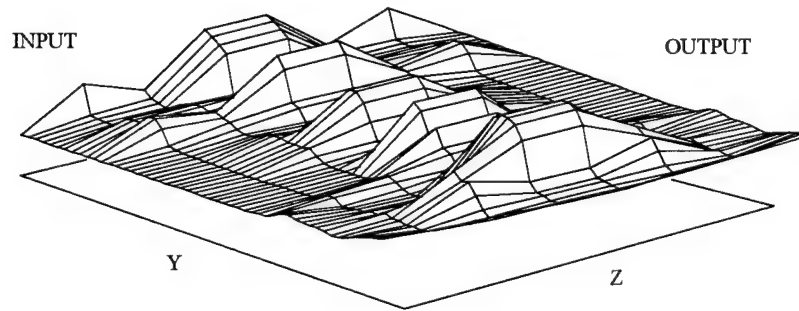


(c)

**Fig. 1** (a) Configuration (top view) of the circular CFA showing the electron drift region and the segmented end-hats. (b) Configuration (cut-away view) of the circular CFA with segmented end-hats and *in situ* probe.



(a)



(b)

**Fig. 2** (a) An example of the Y-Z plane density contour plot at  $X = 0.6$  cm, which is close to the sole, and without RF drive.  $V_{eh} = -1.0$  kV,  $V_{sole} = -1.35$  kV. (b) A mesh plot of the density distribution corresponding to (a).

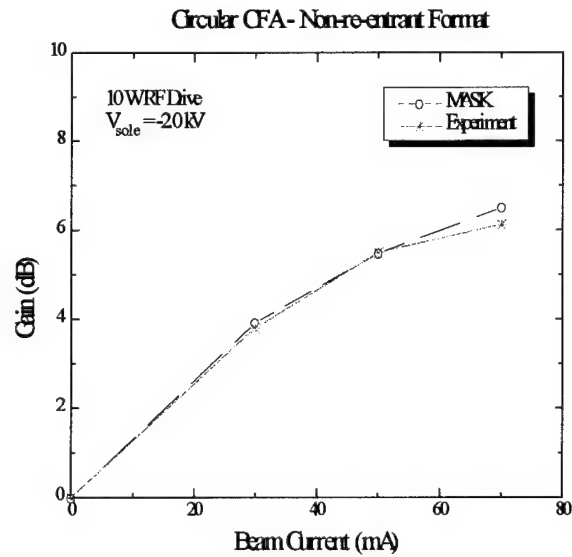


**Fig. 3** Reentrant CFA, comparison between the experiment and simulation - gain versus injected beam current.

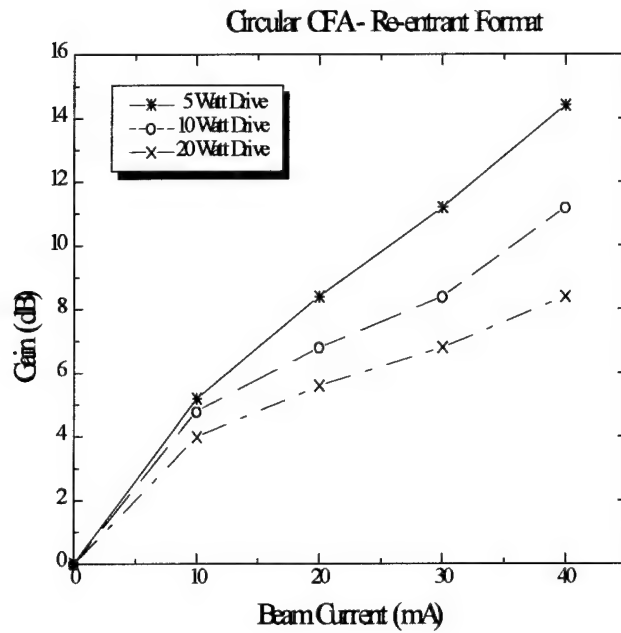


Fig. 4 Reentrant CFA gain as a function of beam current, for different RF drive levels.

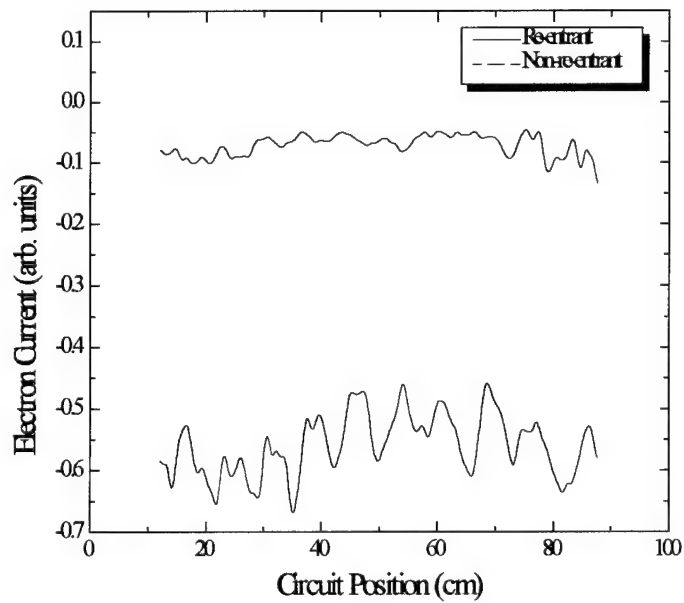
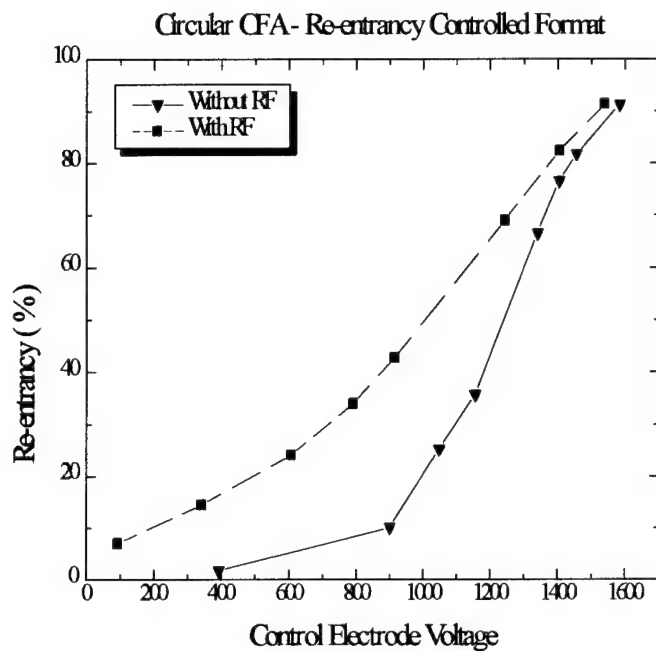
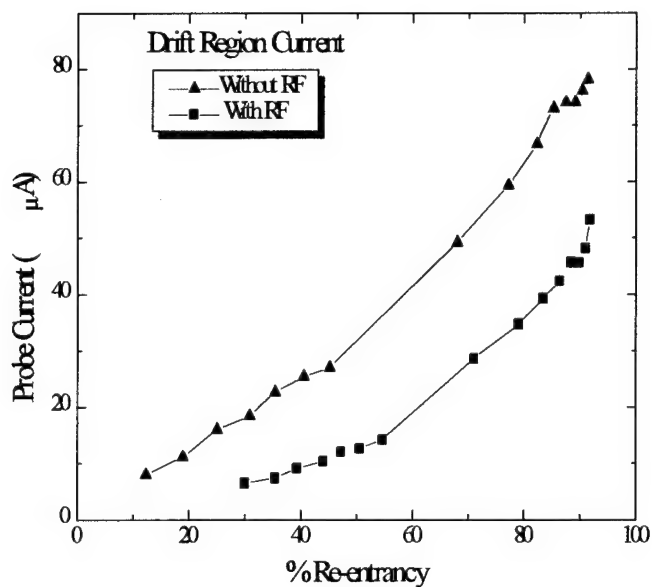


Fig. 5 An example of electron density profile in the reentrant CFA.



**Fig. 6** The degree of reentrancy as a function of the controlled electrode voltage.



**Fig. 7** Electron density variation as a function of reentrancy, measured through an electron density probe in the middle of the beam.

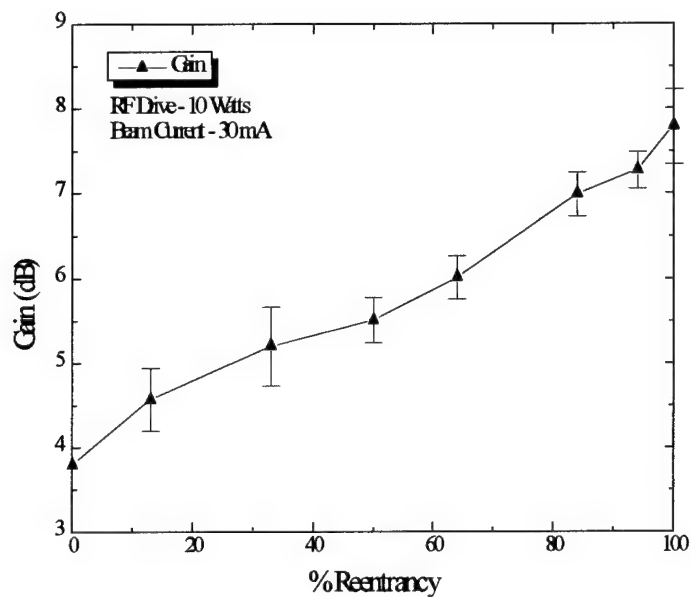


**Fig. 8** Reentrant CFA gain as a function of reentrancy.

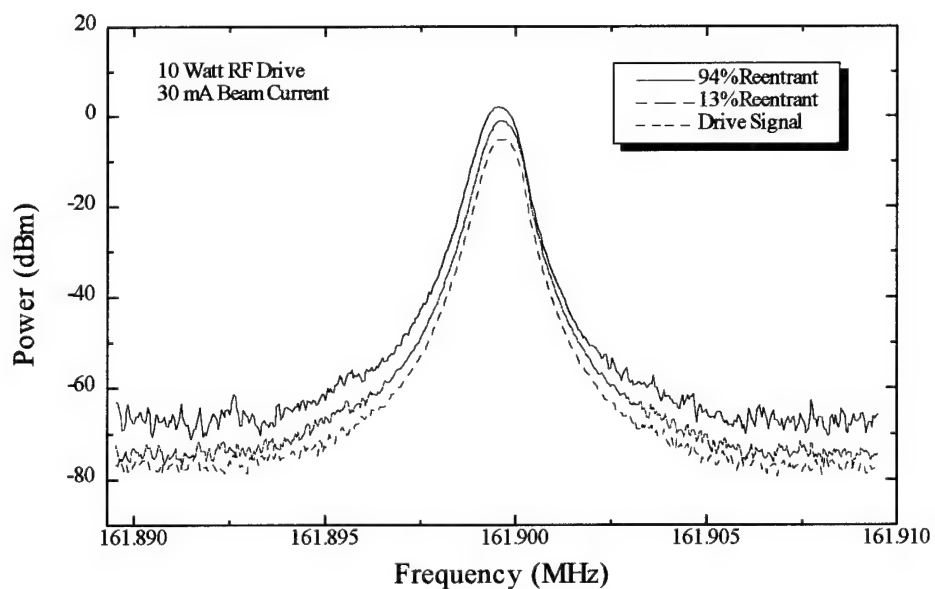


**Fig. 9** The spectrum of circuit output for 94%, 13% reentrancy and the original RF drive signal.



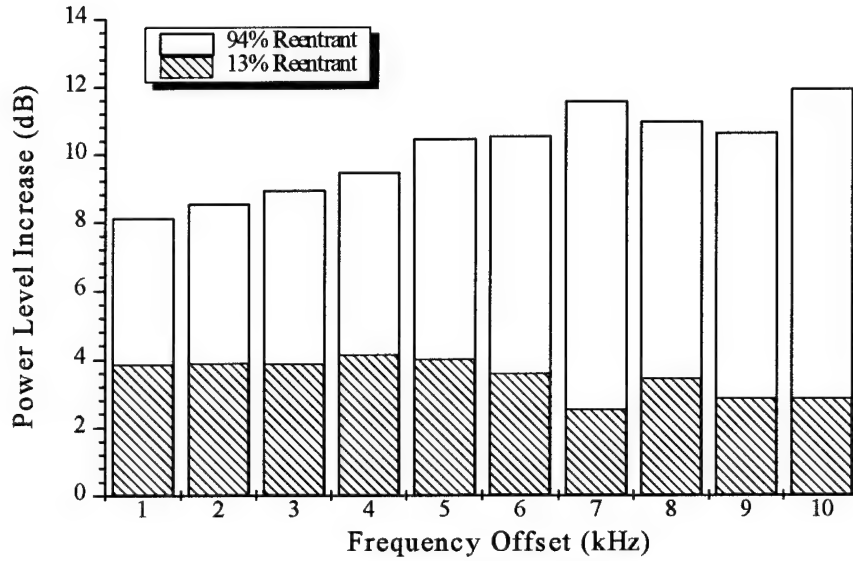


**Fig. 10** The increase of signal/noise power comparing to the RF drive at 94% and 13% reentrancy.

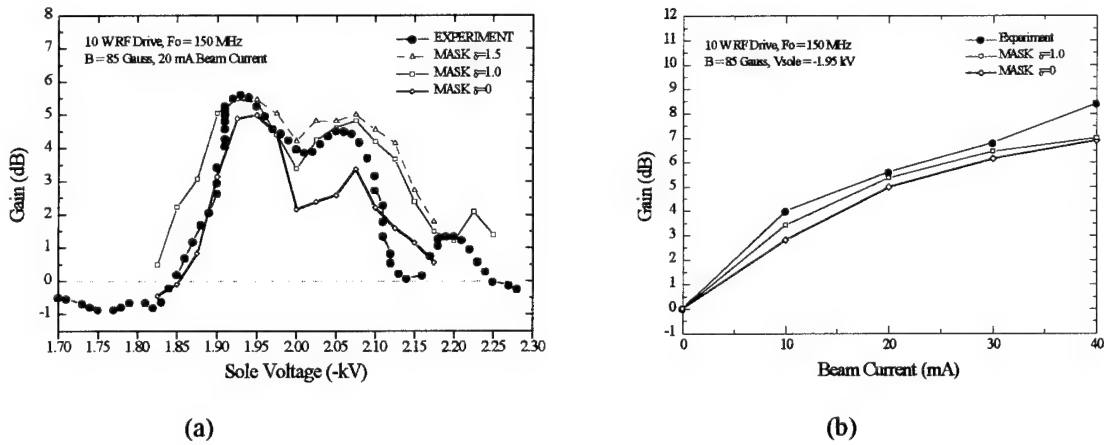


**Fig. 11** (a) A comparison of device electronic gain versus sole voltage operating in the fully reentrant configuration. MASK simulations have been performed for three different values of secondary yield. (b) A comparison of device electronic gain versus beam current operating in the fully reentrant configuration. MASK simulations have been performed for two different values of secondary yield.

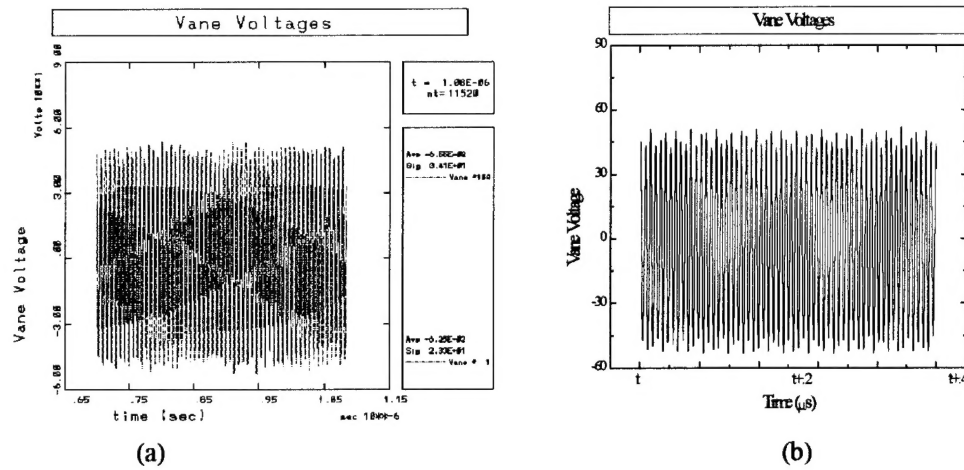


**Fig. 12** Amplifier output waveforms a) simulation, b) experiment.

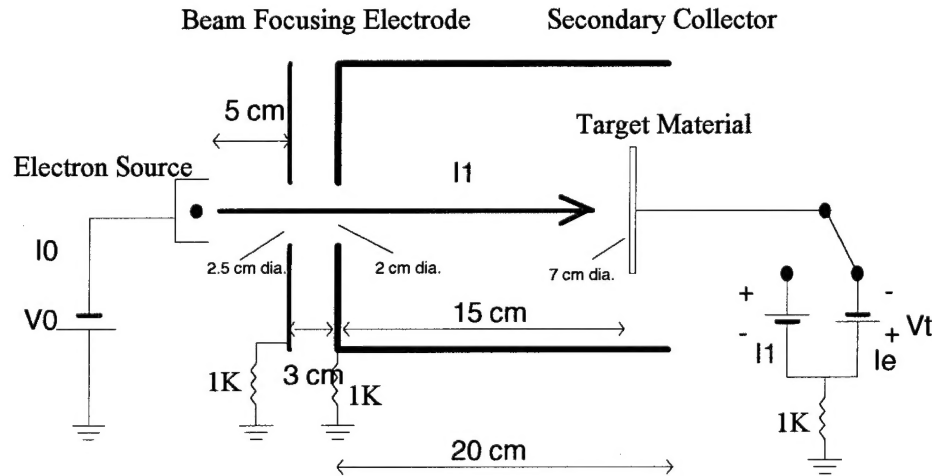


**Fig. 13** Experimental configuration for secondary emission evaluation. The primary beam current collected by the target is obtained by switching the bias of the target more positive with respect to the secondary collector. The net emitting current is obtained by biasing the target more negative with respect to the secondary collector.

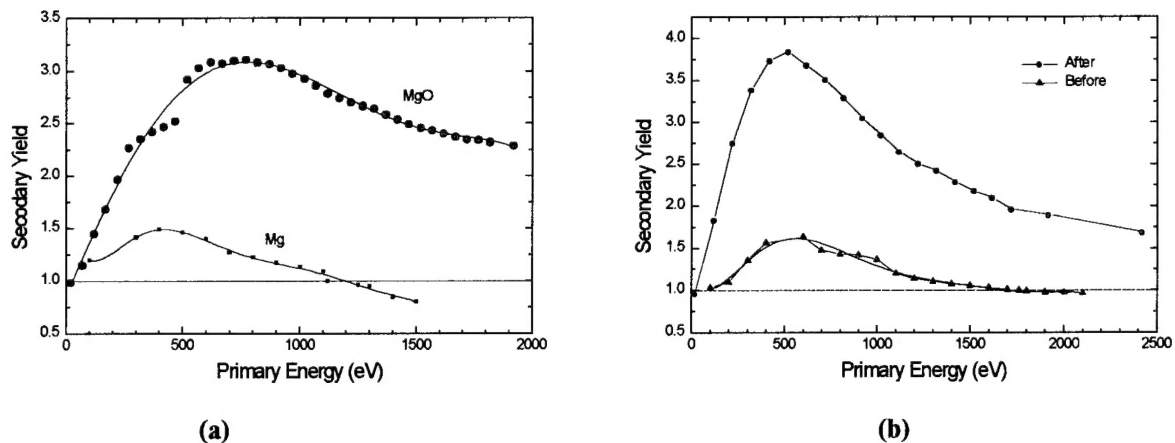


**Fig. 14** (a) Secondary yield measurements for Mg, before (Mg) and after (MgO) the high temperature oxygen treatment. (b) Secondary yield measurements for BeCu, before and after the 4 hour oxygen plasma treatment.

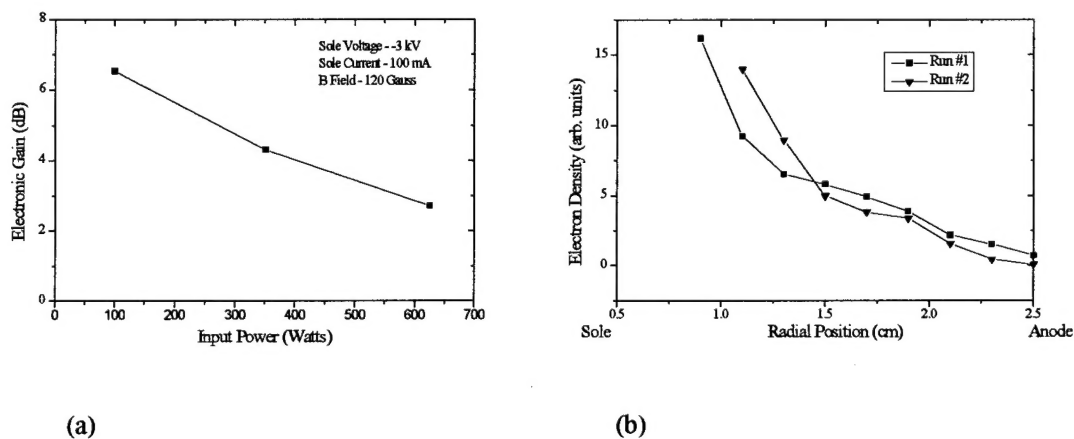
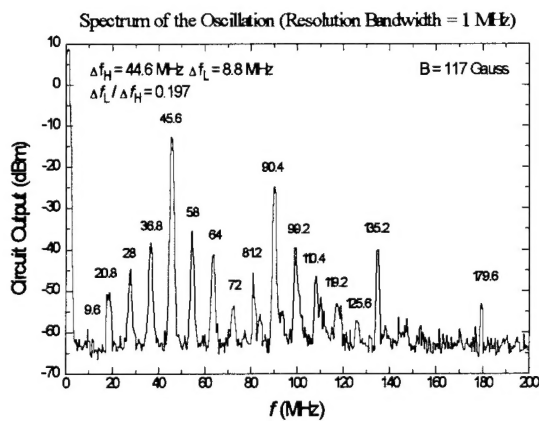
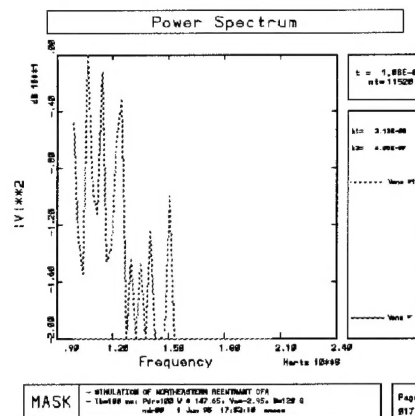


**Fig. 15** (a) Device electronic gain versus input power. (b) Radial electron density measurements taken near output segment of device. This shows the existence of an electron hub as we move to within 1 cm from the sole.



(a)



(b)

Fig. 16 (a) Experimental output spectrum without RF drive (b) MASK output spectrum without RF drive.

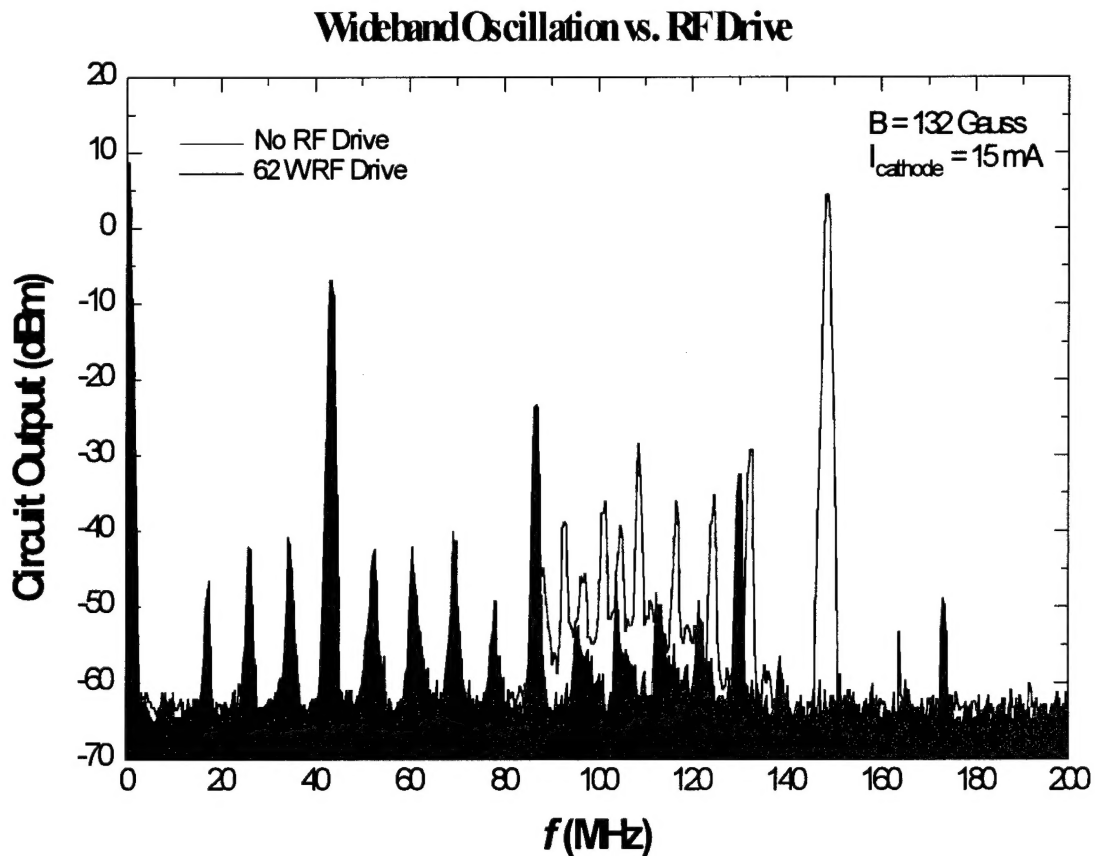
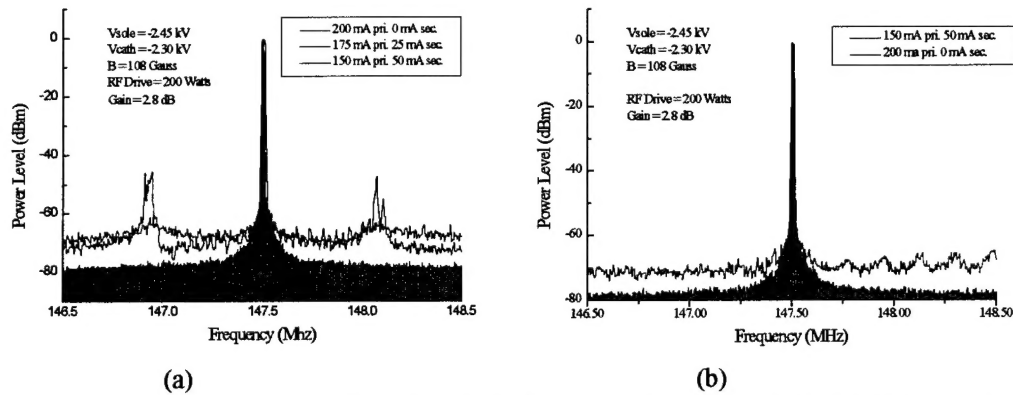
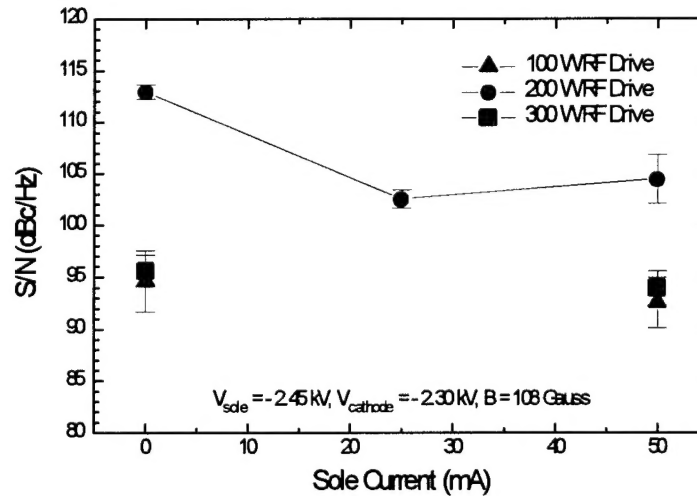


Fig. 17 The effect of 62 watts of RF drive on the out put spectrum.



**Fig. 18** (a) Output spectrum for three cases, 1) 0 mA secondary electron current (shaded region), 2) 25 mA secondary electron current (sidebands starting to form), and 3) 50 mA secondary electron current (distinct sideband spikes). (b) Output spectrum, with parallel capacitor, for two cases, 1) 0 mA secondary electron current (shaded region), 2) 50 mA secondary electron current (sidebands have been suppressed).



**Fig. 19** Calculated signal-to-noise ratio based on the measured spectrum as a function of RF drive level and sole secondary emission.